

PAPER • OPEN ACCESS

## In-field performance and flux pinning mechanism of pulsed laser deposition grown $\text{BaSnO}_3/\text{GdBa}_2\text{Cu}_3\text{O}_{7-\delta}$ nanocomposite coated conductors by SuperOx

To cite this article: M Lao *et al* 2019 *Supercond. Sci. Technol.* **32** 094003

View the [article online](#) for updates and enhancements.









**IOP | ebooks™**

Bringing you innovative digital publishing with leading voices to create your essential collection of books in STEM research.

Start exploring the collection - download the first chapter of every title for free.

# In-field performance and flux pinning mechanism of pulsed laser deposition grown BaSnO<sub>3</sub>/GdBa<sub>2</sub>Cu<sub>3</sub>O<sub>7-δ</sub> nanocomposite coated conductors by SuperOx

M Lao<sup>1</sup> , R Willa<sup>2</sup> , A Meledin<sup>3,4</sup>, H Rijckaert<sup>5</sup> , V Chepikov<sup>6</sup>, S Lee<sup>7</sup>, V Petrykin<sup>7</sup>, I Van Driessche<sup>5</sup> , A Molodyk<sup>6</sup> , B Holzapfel<sup>1</sup> and J Hänisch<sup>1</sup> 

<sup>1</sup>Institute of Technical Physics, Karlsruhe Institute of Technology, Hermann-von-Helmholtz-Platz 1, D-76344 Eggenstein-Leopoldshafen, Germany

<sup>2</sup>Institute for Theory of Condensed Matter, Karlsruhe Institute of Technology, Karlsruhe D-76131, Germany

<sup>3</sup>Central Facility for Electron Microscopy (GFE), RWTH Aachen University, Aachen, Germany

<sup>4</sup>Ernst Ruska-Centre for Microscopy and Spectroscopy with Electrons (ER-C) Forschungszentrum Jülich GmbH D-52428 Jülich, Germany

<sup>5</sup>Department of Chemistry, Ghent University, Krijgslaan 281 (S3), B-9000 Ghent, Belgium

<sup>6</sup>SuperOx, Moscow, Russia

<sup>7</sup>SuperOx Japan LLC, Sagamihara, Japan

E-mail: [mayraluna.lao@kit.edu](mailto:mayraluna.lao@kit.edu)

Received 12 March 2019, revised 17 May 2019

Accepted for publication 18 June 2019

Published 24 July 2019



CrossMark

## Abstract

We investigate the field, angle and temperature dependence of the full-width critical current,  $I_c$ , of pulsed laser deposition-grown GdBa<sub>2</sub>Cu<sub>3</sub>O<sub>7</sub> coated conductors with and without additional 6 mol% BaSnO<sub>3</sub> (BSO) nanoparticles fabricated by SuperOx. The transport characteristics measured from 7 to 77 K and in applied magnetic fields of up to 6 T are complemented by scanning transmission electron microscopy. This combined approach allows for further insight into the vortex pinning mechanism and helps with understanding the enhancement in  $I_c$ . An exemplary scaling of the pinning force curves versus field at different temperatures confirms the additional contribution to pinning by the BSO nanoparticles. Through the temperature dependence of  $I_c$ , the weak and strong pinning contributions are determined: strong pinning dominates over almost the entire temperature range especially near the matching field of 1 T, where the largest enhancement in  $I_c$  is achieved.

Keywords: coated conductors, GdBCO, critical current, vortex pinning

(Some figures may appear in colour only in the online journal)

## 1. Introduction

Various forms of physical defects in superconducting REBa<sub>2</sub>Cu<sub>3</sub>O<sub>7-δ</sub> (REBCO, RE = rare earth) films have been found to pin vortices and to effectively enhance the critical



Original content from this work may be used under the terms of the [Creative Commons Attribution 3.0 licence](https://creativecommons.org/licenses/by/3.0/). Any further distribution of this work must maintain attribution to the author(s) and the title of the work, journal citation and DOI.

**Table 1.** Summary of the coated conductor samples.

Sample name	Secondary phase	Deposition rate (nm min <sup>-1</sup> )	BSO nanorod diameter (nm)	$I_{c,sf}$ at 77 K (A)	$T_c$ (K)
Reference	—	750	—	219	93.1
APC-375	6 mol% BSO	375	5.3 ± 2.1	141	92.1
APC-560	6 mol% BSO	560	8.3 ± 4.0	125	92.3

current density,  $J_c$ , for reviews see [1, 2]. These physical defects are a few nanometer in size and are either related to the deposition process such as grain boundaries, oxygen vacancies, and dislocations or artificially introduced, e.g. nanosized precipitates that form by addition of secondary phases. Many studies have already shown that by adding secondary phases,  $J_c$  of REBCO films can be increased dramatically [2–5]. In addition, the anisotropy of  $J_c$  with regard to the direction of the applied magnetic field can be reduced. Therefore, it is very tempting for coated conductor manufacturers to incorporate artificial pinning centers (APC) using secondary phases to improve the in-field performance of their tapes [6–8]. From a technological perspective, it is important to optimize the critical current  $I_c$ , rather than the current density  $J_c$ , and to tailor it for a specific target operating temperature.

Recently, SuperOx performed initial investigations on adding perovskite APC in the form of BaSnO<sub>3</sub> (BSO) and BaZrO<sub>3</sub> (BZO) using their high-rate production process [9]. Different molar percentages and deposition rates were explored with the goal to optimize the process for largest  $I_c$  especially at low temperatures. In their initial results, samples with additional BSO secondary phase showed the most significant enhancement of  $I_c$ .

We investigated in detail the field, temperature and angle dependence of the critical current,  $I_c(B, T, \theta)$ , of APC-added tapes from SuperOx at intermediate temperatures between liquid helium (4.2 K) and liquid nitrogen (77 K) temperatures and at moderate fields of up to 6 T. The electrical characterization is complemented by scanning transmission electron microscopy (STEM) analysis to understand the vortex pinning mechanism in these BSO-added tapes.

## 2. Materials and methods

The fabrication process of the coated conductor samples, produced by SuperOx, consists of pulsed laser deposition (PLD) of GdBa<sub>2</sub>Cu<sub>3</sub>O<sub>7- $\delta$</sub>  (GdBCO) on an ion beam assisted deposition (IBAD)-textured Hastelloy substrate. Details of the processing technique are discussed in [10]. In this work, we focus on three samples, whereof one is a reference sample with pure GdBCO layer. The other two samples have an additional BSO secondary phase. The two samples with APC were grown at different deposition rates, 375 and 560 nm min<sup>-1</sup> and are consequently abbreviated by APC-375 and APC-560. All three tapes have a width of 6 mm and a GdBCO thickness of 1.1  $\mu$ m. The critical temperature  $T_c$ , of

the APC-containing samples are only slightly lower than the reference tape (table 1).

The  $V(I)$  curves of the full-width coated conductor samples were measured using a high-current electrical characterization system [11]. The samples were mounted in a He gas flow cryostat with a 6 T split coil magnet. A rotation stage enables a continuous rotation of the sample with respect to an applied field (we focus on a 200° angular range). Further details about the experimental setup were discussed in [11]. The critical current was evaluated by fitting a power law function of the form  $V(I) = V_c \left(\frac{I}{I_c}\right)^N$ , where  $V_c = 1.8 \mu$ V is the voltage criterion derived from an electric field criterion,  $E_c = 0.5 \mu$ V cm<sup>-1</sup>.

The composition and structure of the defects in the superconducting layers were analyzed using STEM technique. In this work, different STEM devices were used: a  $C_s$ -corrected JEOL JEM 2200-FS instrument operated at 200 kV was used for the reference SuperOx sample. The samples for STEM were prepared by cutting a cross-sectional and a planar-view lamella via the focused ion beam (FIB) technique in an FEI Nova 600 Nanolab Dual Beam FIB scanning electron microscope [12]. The lamellae were extracted using the *in situ* lift out procedure with an Omniprobe extraction needle. Prior to FIB preparation, an etching step with mecbrite CA-92 was introduced to remove 20  $\mu$ m copper stabilizer. For the samples with APC, we carried out the annular dark field STEM and high angle annular dark field (HAADF) STEM together with energy dispersive x-ray spectroscopy (EDX). The experiments involved an FEI Titan g2 80–200 Crewley microscope operated at 200 kV and equipped with a ‘Super-X’ wide solid angle EDX detector [13].

## 3. Results

### 3.1. Microstructure

Secondary phases such as Gd<sub>2</sub>O<sub>3</sub> and BaCeO<sub>3</sub> were found in a typical cross-section TEM images of a standard SuperOx sample as shown in figure 1(a). The Gd<sub>2</sub>O<sub>3</sub> precipitates occasionally reach up to a few hundred nanometers in diameter as further shown in the EDX mapping in figure 1(b). On the other hand, the BaCeO<sub>3</sub> particles are outgrowths that form at the interface of GdBCO and the CeO<sub>2</sub> buffer layer. Additional defects in the superconducting matrix include vertical grain boundaries and stacking faults parallel to the *ab*-planes with strained regions.

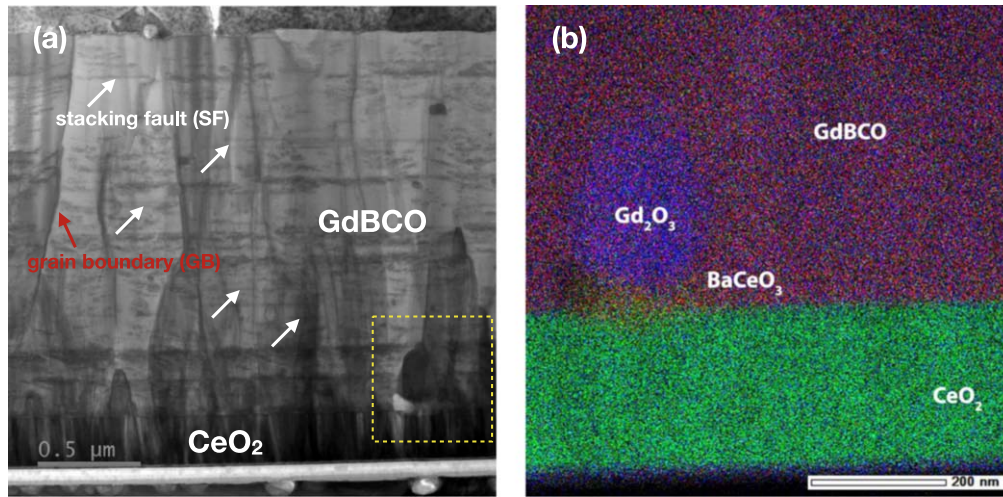


**Figure 1.** HAADF image cross-sectional of the standard tape of SuperOx. (b) EDX mapping of the boxed region in (a) which shows the  $Gd_2O_3$  and  $BaCeO_3$  phases.

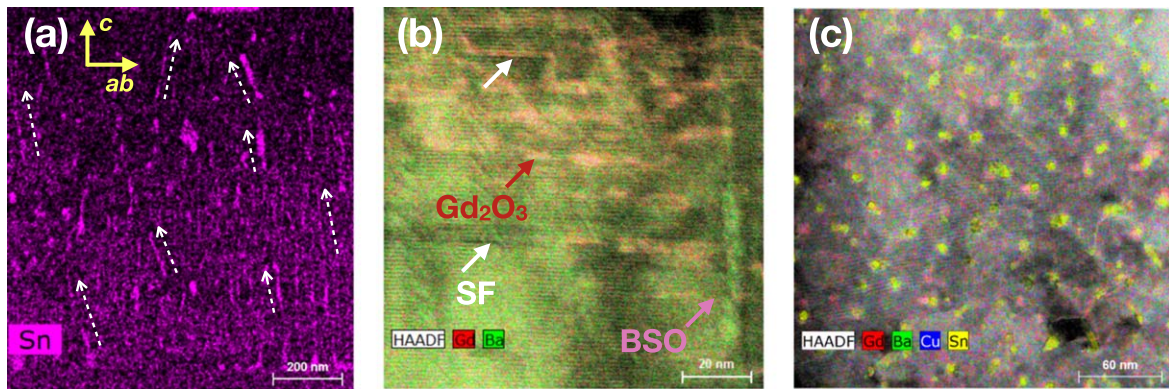


**Figure 2.** (a) Elemental Sn STEM-EDX map of a cross-sectional sample. (b) Composite image of HAADF STEM image and elemental Gd and Ba EDX maps of a cross-sectional sample. (c) Composite image of HAADF STEM image and elemental Gd, Ba, Cu and Sn EDX maps of a plan view sample.

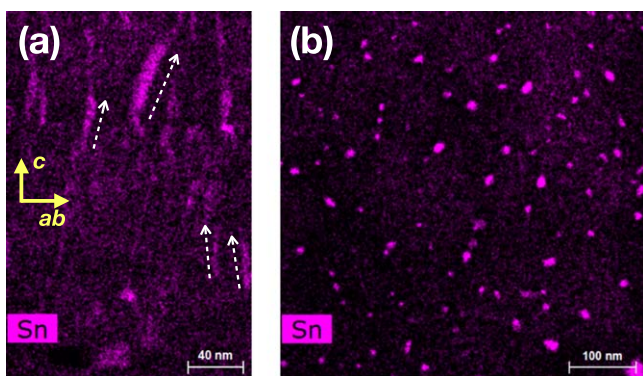


**Figure 3.** Elemental Sn EDX maps of the (a) cross-section and (b) planar view of the surface of APC-560.

For the APC-375, the cross-sectional HAADF image clearly shows BSO nanoparticles in the form of rods with lengths of about 180–200 nm (figure 2). The nanorods grow with a slight tilt from the  $c$ -axis direction indicated by the

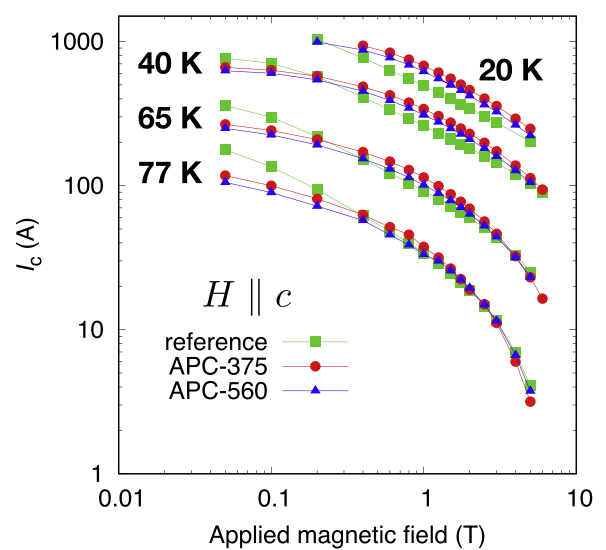


**Figure 4.** Field dependence of  $I_c$  of the tapes at several temperatures for  $H||c$ .

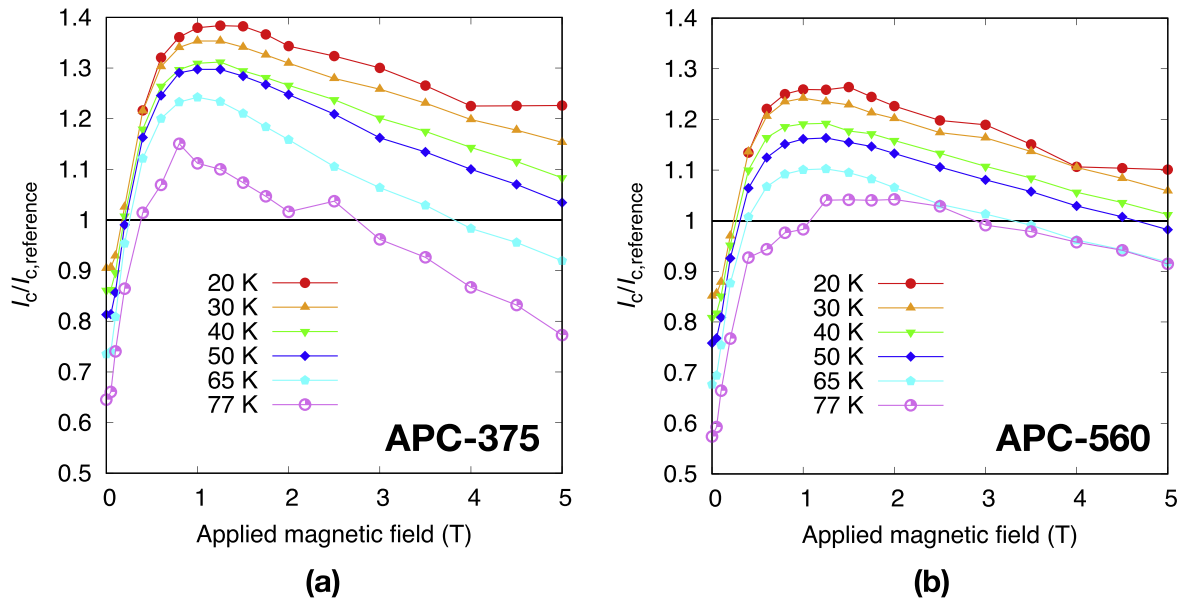


**Figure 5.**  $I_c$  enhancement with field in different temperatures from 20 to 77 K for (a) APC-375 and (b) APC-560.

arrows in figure 2(a). We also find  $\text{Gd}_2\text{O}_3$  nanoparticles slightly elongated along the  $ab$ -planes (figure 2(b)). Using the planar images shown in figure 2(c), planar density and diameter of the BSO nanorods are estimated to  $480 \mu\text{m}^{-2}$  and  $5.3 \pm 2.1 \text{ nm}$ , respectively.

The APC-560 sample shows a similar columnar form of BSO, figure 3(a). The planar density is estimated to  $480 \mu\text{m}^{-2}$  which is the same as for APC-375. The similarity in the density of the BSO nanoparticles between the APC samples having the same amount of additional 6 mol% BSO is due to opposing trends of particle diameter and length in the two samples. The diameter of the rods in the APC-560 sample is about  $8.3 \pm 4.0 \text{ nm}$ , and hence slightly larger than in the APC-375 sample. Meanwhile, the rods lengths, in the range of 40–80 nm, is smaller. This effect is attributed to the higher deposition rate, which is unfavorable for growing long nanorods. This observation is consistent with the 3D Monte-Carlo simulations by Ichino *et al* on the nanorod self-organization in REBCO films grown by vapor phase epitaxy [14]. This sample contains less  $\text{Gd}_2\text{O}_3$  nanoparticles compared to APC-375. Aside from the secondary phases, the APC-added samples also contain stacking faults and grain boundaries. Based on the planar density of the BSO nanorods, the matching field,  $B_\phi$ , which is defined as the field at which the density of the pinning centers equals the density of the vortices, can be calculated:  $B_\phi = \phi_0/d^2 = n_p\phi_0$ , where  $\phi_0$  is the magnetic flux quantum,  $d$  is the (planar) average spacing between the vortices and  $n_p$  is the normalized defect density. For the estimated density of the BSO nanorods from the STEM images (figures 2 and 3),  $B_\phi$  is about 1 T for both APC-375 and APC-560.

### 3.2. Transport properties

The samples with APC have a lower self-field  $I_c$  than the reference sample, figure 4, which is common for PLD films with secondary phases. At 77 K, a net enhancement in  $I_c$

(defined relative to  $I_c$  of the reference sample) in APC-containing tapes is observed in the range of about 0.5–3 T (figure 5). As the temperature decreases, the net  $I_c$  enhancement as well as its field range increases. The maximum  $I_c$  enhancement is achieved at a field of approximately 1 T for both APC samples and this agrees with the matching field evaluated from the planar density of the nanorods. APC-375 consistently has larger  $I_c$  enhancement for  $H\parallel c$  than APC-560, reaching about 40% at 20 K while the latter has about 30% increase with respect to the reference sample.

The trend is also observed in the angular dependence of the critical current at different temperatures and fields, figure 6. For the reference sample (green line), two peaks are observed: (i) a large  $ab$ -peak due to intrinsic pinning and correlated pinning centers parallel to the  $ab$ -planes (i.e. stacking faults) and (ii) a small peak at  $0^\circ$  which appears due to planar grain boundaries and dislocation cores. The  $ab$ -peak is slightly shifted by about  $3^\circ$  from the direction parallel to the tape ( $\pm 90^\circ$ ), which is commonly observed in IBAD tapes due to basal dislocations as observed in STEM analysis (not shown here). The small  $c$ -axis peak is more visible at 77 and 50 K and becomes less discernible at 30 K.

At 77 and 50 K (first and second column of figure 6), the APC samples also have two characteristic peaks: (i) the  $ab$ -peak that is also slightly shifted from  $\pm 90^\circ$  and (ii) an asymmetric peak that is at around  $+10^\circ$  in the APC-375 and  $-10^\circ$  in the APC-560 moving towards the  $ab$ -direction for decreasing fields. The asymmetric peak is a consequence of the inclined growth of the BSO nanorods found in the STEM images (figures 2 and 3). As a common effect of additional pinning centers, the anisotropy of  $I_c$ , defined as the ratio between  $I_c(H\parallel ab)$  and  $I_c(H\parallel c)$ , is also evidently reduced in the APC samples. The reference sample shows the sharpest  $ab$ -peak and the highest  $I_c$  values near  $H\parallel ab$ , so the APCs only lead to an increased  $I_c$  for angles away from the  $ab$ -plane direction. At 30 K (third column in figure 6), the asymmetric

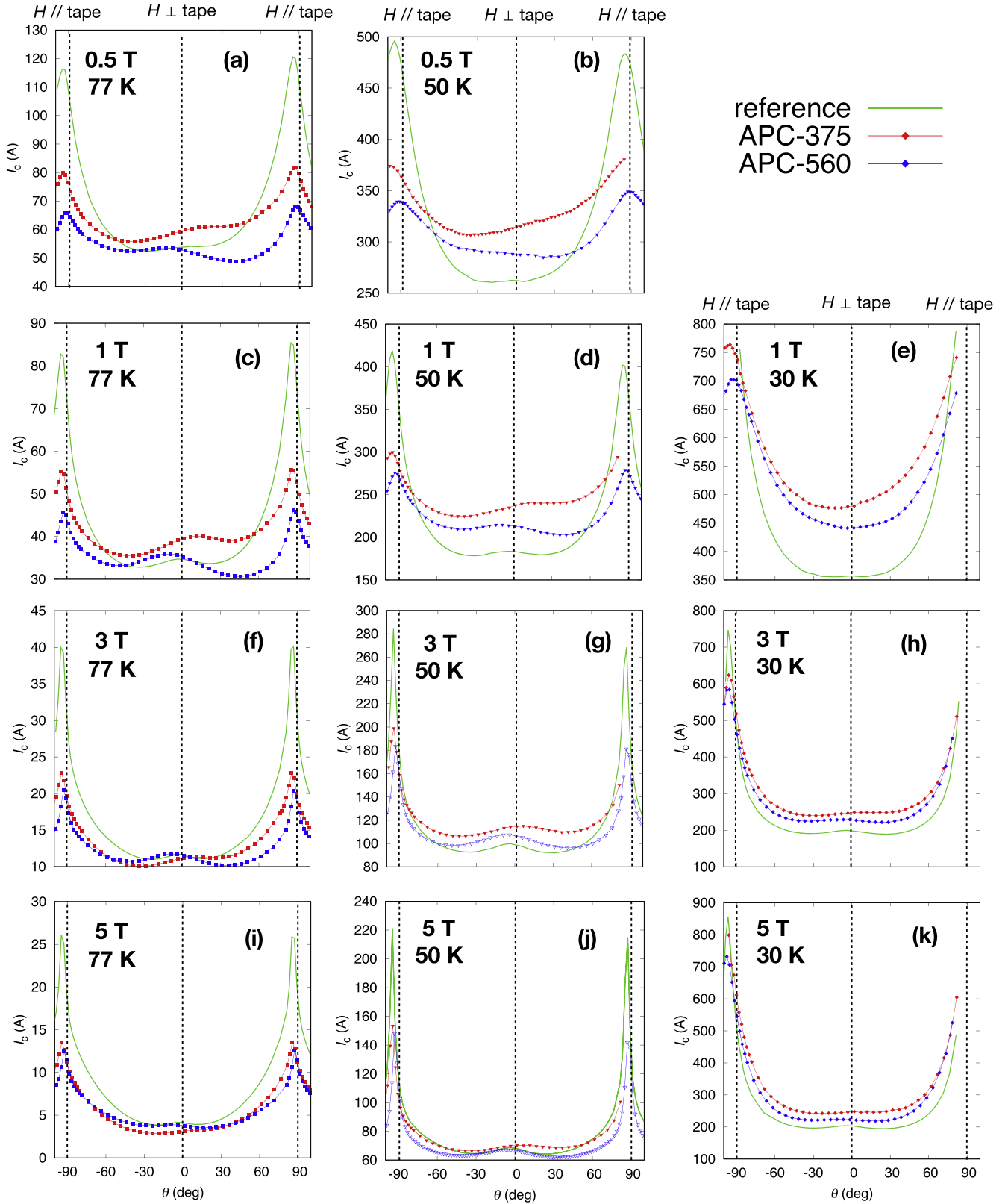


**Figure 6.** Angle dependence of  $I_c$  at applied fields of (a), (b) 0.5 T, (c)–(e) 1 T, (f)–(h) 3 T and (i)–(k) 5 T at 77 K (left), 50 K (middle) and 30 K (right).

peak appears to be smeared out but the APC samples remain to have a higher  $I_c$  compared to the reference sample except near the direction of the  $ab$ -planes.

The minimum critical current,  $I_{c,\min}$  which determines the limit in the operating current for application, is also improved in certain fields and temperatures in the APC samples.  $I_{c,\min}$

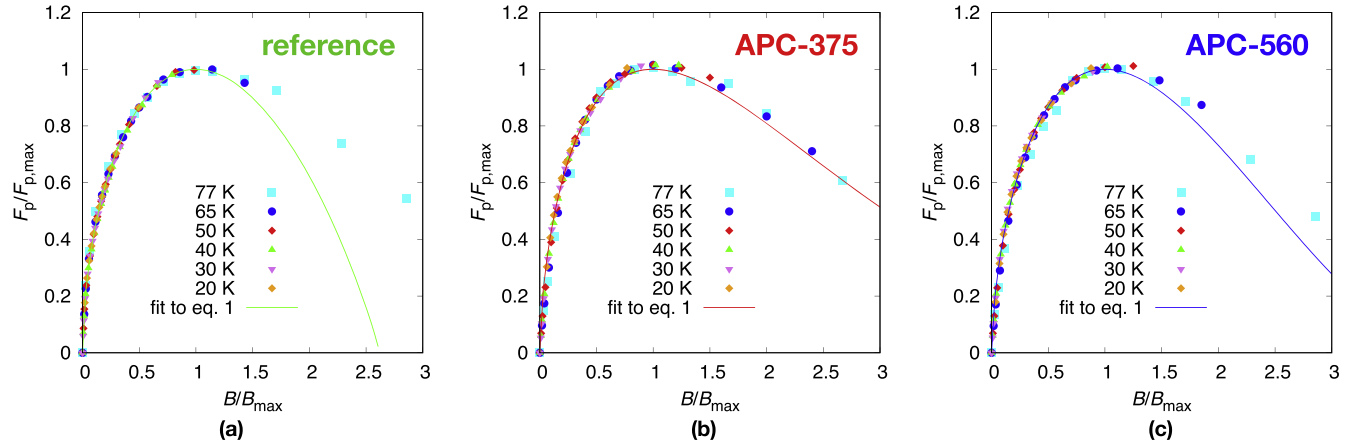


**Figure 7.** Normalized pinning force density versus normalized applied magnetic field for the (a) reference sample, (b) APC-375 and (c) APC-560 at different temperatures.

**Table 2.** Fitting parameters from equation (1) including  $B_{\max}$  and  $F_{p,\max}$ .

Sample name	$p$	$q$	$\alpha$	$B_{\max}$ (T) at 77 K	$B_{\max}$ (T) at 20 K	$F_{p,\max}$ (GN m <sup>-3</sup> ) at 20 K
Reference	0.55	0.89	0.45	1.75	10.1	177
APC-375	0.59	6.00	0.41	1.5	6.5	187
APC-560	0.60	1.90	0.40	1.75	5.7	168

occurs at  $\pm 30^\circ$  in the reference tape,  $-45^\circ$  in APC-375 and  $+45^\circ$  in APC-560. With respect to the reference sample, APC-375 has higher  $I_{c,\min}$  at 1 and 3 T while APC-560 even has lower  $I_{c,\min}$ . As the temperature decreases,  $I_{c,\min}$  of both APC samples surpasses  $I_{c,\min}$  of the reference depicting additional pinning which leads to improvement in  $I_c$  by the BSO nanorods even for angles away from the main orientation of the rods. However, the enhancement is still strongly influenced by matching effects where maximum  $I_c$  enhancements can be achieved for fields close to 1 T.

## 4. Discussion

### 4.1. Pinning force density

To further understand the governing mechanism responsible for the increase in  $I_c$ , one can consider its field-dependence, i.e.  $I_c(B)$ . Depending on the vortex pinning regime, the behavior of  $I_c(B)$  may vary. In certain limits, the field dependence is shown to follow a power law  $I_c(B) \propto B^{-\alpha}$ , and the exponent  $\alpha$  has been evaluated by analytic or numerical means. As commonly observed in REBCO films with secondary phases, the  $I_c(B)$  curve appears to be rather rounded, see figure 4. Consequently, a reliable extraction of the exponent  $\alpha$  turns out delicate. To circumvent this difficulty, we use the Dew-Hughes-type functions for the field dependence of the pinning force density,  $F_p(B)$  (modified for high-temperature superconductors) by replacing the upper critical field,  $B_{c2}$ , by irreversibility field,  $B_{irr}$ :  $F_p(b_i) = Kb_i^p(1 - b_i)^q$ , where  $K$  is constant,  $b_i = B/B_{irr}$  is the reduced field and the variables  $p$  and  $q$  are parameters that are associated to the flux pinning mechanism in the original model [15]. This type of functions (i.e. a beta

distribution) follows easily from statistical considerations [16, 17] or (with the glass-liquid transition as scaling field) from a percolation model [18]. Because the actual  $H_{irr}$  value is difficult to determine especially at lower temperatures, the data were scaled here by  $F_{p,\max}$  and  $B_{\max} = B(F_{p,\max})$ . After rescaling the data, figure 7, a simple fit according to

$$f_p(b) = \frac{F_p(b)}{F_{p,\max}(b)} = \left(\frac{p}{q}\right)^q b^p \left(\frac{p+q}{p} - b\right)^q, \quad (1)$$

where  $b = B/B_{\max}$  provides values for the fitting parameters  $p$  and  $q$ . As a first-order approximation, the value of  $p$  is related to the exponent  $\alpha$  via  $\alpha = 1 - p$  [19]. The values of  $p$ ,  $q$  and  $\alpha$  together with corresponding  $B_{\max}$  and  $F_{p,\max}$  values at 77 and 20 K are listed in table 2.

Since the peak in  $F_p(b)$  is not observable for  $T < 50$  K due to the limited field range of the measurements, this study puts more emphasis on the increasing part of  $f_p(B)$  where equation (1) fits quite well and mostly influences the value of  $p$ . On the other hand, the deviation of the fit in the high-field region may be due to the large flux creep [20] at  $T > 50$  K, which is not described by equation (1). Thus, the values of  $q$  obtained from the fit are deemed acceptable but will not be used for the analysis of pinning.

The fact that the increasing parts of  $f_p(b)$  collapse into one curve in all the samples implies that a common pinning mechanism governs  $I_c$  in these temperatures and fields. The values of  $\alpha$  calculated from the parameter  $p$  for APC-375 and APC-560 are very close and are only slightly smaller than the reference sample. The decrease in the value of  $\alpha$  is commonly observed when the pinning landscape becomes more disordered. Various studies have used the framework of bulk time-dependent Ginzburg–Landau (TDGL) simulations for

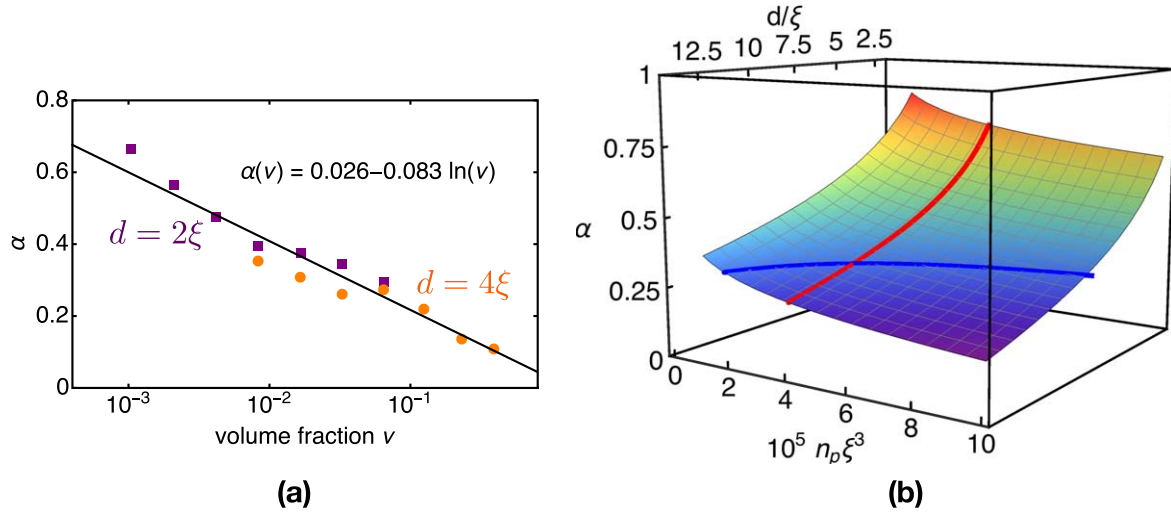


**Figure 8.** (a)  $\alpha$  value as a function of the volume fraction of the non-superconducting inclusions for  $d = 2\xi$  and  $4\xi$ . (b) Surface plot of  $p = 1 - \alpha$  as a function of defect size and normalized defect density fraction  $n_p \xi^3$ . The blue line represents a volume fraction of 2.5% and the red line corresponds to  $n_p \xi^3 = 4e - 5$ .

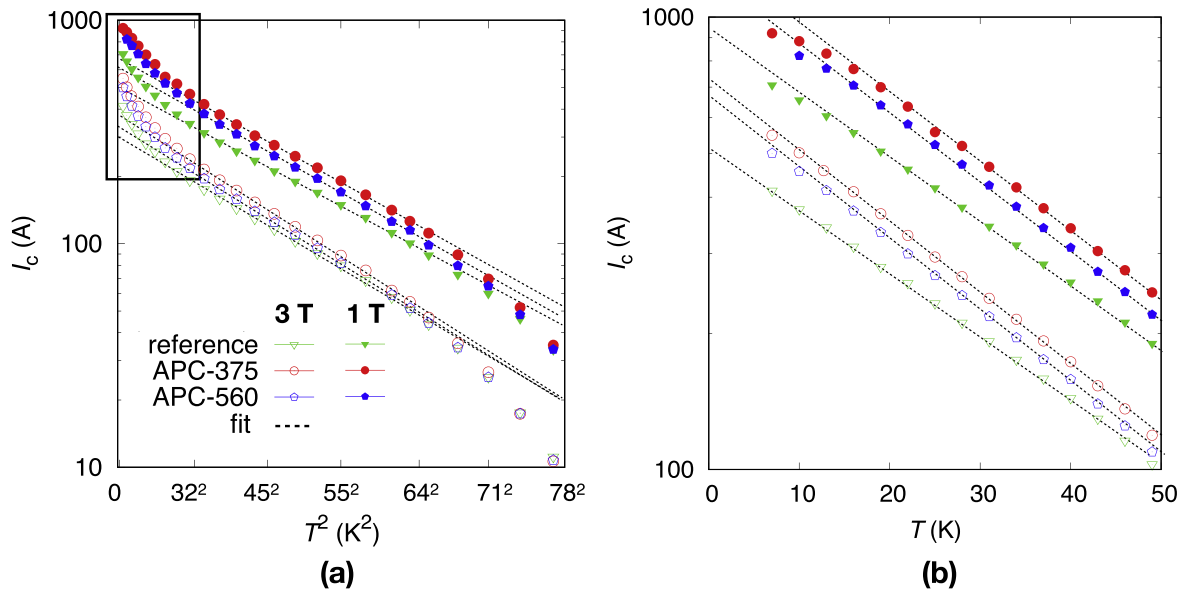


**Figure 9.** (a)  $\log(I_c)$  versus  $T^2$  at 1 and 3 T. (b)  $\log(I_c)$  versus  $T$  at 1 and 3 T corresponding to the temperature range in the boxed region in (a).

the superconducting order parameter to gain more insight in the pinning mechanism related to the values of  $\alpha$  [21–24]. According to the simulation results of Paturi *et al* [19], the value of the parameter  $p$ , and subsequently  $\alpha$ , depends on the diameter of the pinning center. On the other hand, by implementing a large-scale simulation solving TDGL equations for a three dimensional system [21],  $\alpha$  was found to be largely influenced by the volume fraction of the non-superconducting inclusions,  $\nu = (\pi/6)n_p d^3 [1 - (\pi/12)n_p d^3]$  where  $d$  is the size of the inclusion. As shown in figure 8(a), regardless of  $d$ , the values of  $\alpha$  coincides in the same curve which depends logarithmically with  $\nu$  in that model. In the case of APC-375 and APC-560, the volume fraction of the BSO phase is about 2.5%, which roughly agrees with the  $\alpha$  values listed in table 2. Further illustrated by the blue line in the surface plot of  $d$ ,  $p$

and normalized defect density  $n_p \xi^3$  (figure 8(b)), assuming a constant volume fraction of 2.5%, the  $\alpha$  value does not significantly change as the size of the inclusion changes. On the other hand, when the normalized defect density,  $n_p \xi^3$ , estimated to be about  $4 \times 10^{-5}$  for the samples with BSO nanorods, the  $\alpha$  value would show a significant dependence in  $d$  for changing volume fraction (red line in figure 8(b)). The higher  $\alpha$ -value of the reference sample may be due to a smaller defect size (consider grain boundaries and  $\text{Gd}_2\text{O}_3$  precipitates) and/or a lower volume fraction of inclusions compared with the APC-added tapes. Therefore, the BSO nanorods indeed dominate the vortex pinning within the field and temperature range of the scaled pinning force for fields roughly parallel to  $c$ -axis (or the average nanorod direction). The values of  $B_{\text{max}}$  of the three samples at 77 K are quite close while the reference sample



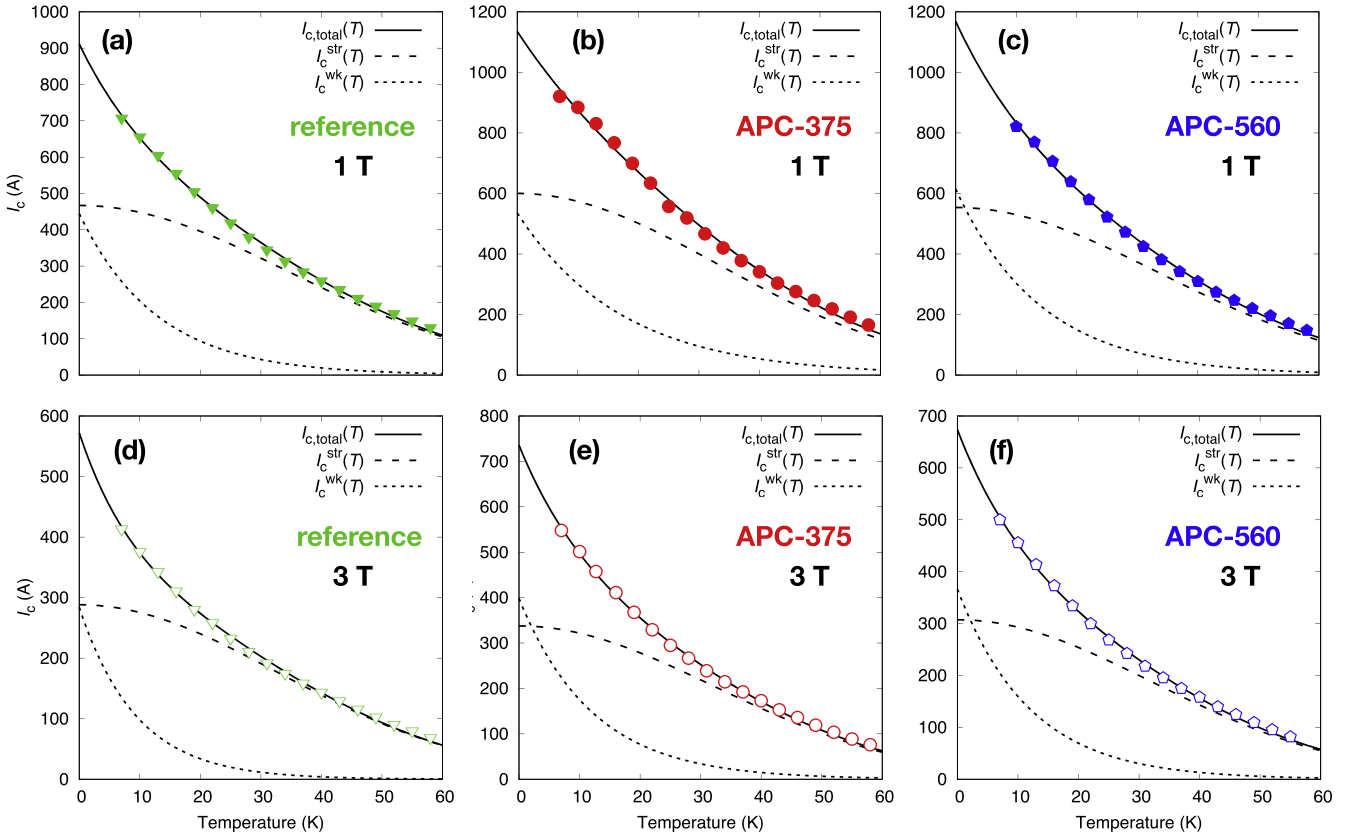


**Figure 10.** Temperature dependence of the weight of the strong and weak pinning contributions according to the obtained  $T_0$ ,  $T^*$ ,  $I_c^{\text{str}}(0)$  and  $I_c^{\text{wk}}(0)$  at (a)–(c) 1 T and (d)–(f) 3 T. The symbols are the  $I_c(T)$  data of figure 9.

gains a much larger value at 20 K than the APC-added tapes. The lower value of  $B_{\text{max}}$  in the APC samples at 20 K is due to matching effects of the BSO nanorods which occurs at 1 T. On the other hand,  $B_{\text{max}}$  of all samples at 77 K as well as for the reference sample at 20 K, is governed via  $p$  and  $q$  by the irreversibility field,  $B_{\text{irr}}$ , where typical  $B_{\text{irr}}$  values of REBCO films at 20 K and 77 K are about 50 T and 6 T, respectively [25, 26].

In order to understand how the BSO nanorods influence the overall pinning behavior, the temperature dependence of  $I_c$  at 1 and 3 T with  $H$  normal to the tape is investigated. For strong pinning of a line disorder,  $I_c(T)$  can be expressed as [27]:

$$I_c^{\text{str}}(T) = I_c^{\text{str}}(0) \exp\left[-3\left(\frac{T}{T^*}\right)^2\right] \quad (2)$$

while for weak pinning of point-like uncorrelated disorder,  $I_c(T)$  takes the form [28]:

$$I_c^{\text{wk}}(T) = I_c^{\text{wk}}(0) \exp\left(-\frac{T}{T_0}\right), \quad (3)$$

where  $T^*$  and  $T_0$  are quantities proportional to the energy scale of the pin and  $T \ll T_c$ .

When  $\log(I_c)$  is plotted versus  $T^2$  according to equation (2), we observe a strong-pinning dominated behavior over a wide temperature range. Deviations from that

behavior are observed at high temperatures due to larger flux creep, and at low temperatures (i.e.  $T < 38$  K), pointing towards a different pinning mechanism. When the temperature dependence is plotted in lin-log scale, the linear behavior expected from equation (3) appears below 40 K suggesting the increasing significance of weak pinning.

Although the contributions of weak and strong defects to the critical current are far from trivial [23, 29], we proceed with a simplified analysis splitting the total critical current into the direct sum of weak-pinning and strong-pinning, i.e.  $I_c(T) = I_{c,\text{total}}(T) = I_c^{\text{str}}(T) + I_c^{\text{wk}}(T)$  where  $I_c^{\text{str}}(T)$  and  $I_c^{\text{wk}}(T)$  are given by equations (2) and (3), respectively. In contrast to the sophisticated analysis of isotropic-strong and anisotropic-strong contribution as implemented by Palau *et al* [30], our analysis uses an averaged strong pinning contribution. The weight of the contributions of the weak and strong pinning is shown in figure 10. The values of  $T_0$  and  $T^*$  resulting from the fit (table 3), are generally higher at 1 T than at 3 T. The behavior and values of  $T^*$  are consistent with the results in [30, 31]. Between the three samples, the tapes with APC have higher  $T_0$  but lower  $T^*$  than the reference.

In this analysis, the parameters  $I_c^{\text{str}}(0)$  and  $I_c^{\text{wk}}(0)$  are understood as the contributions of the strong and weak pinning centers in the absence of flux creep and have earlier been interpreted to be proportional to the density of the defects [30]. From the values obtained from the fits (table 3),

**Table 3.** Fitting parameters from equations (2) and (3).

Sample	$T_0$ (K)		$T^*$ (K)		$I_c^{wk}(0)$ (A)		$I_c^{str}(0)$ (A)	
	1 T	3 T	1 T	3 T	1 T	3 T	1 T	3 T
Reference	12.8	9.4	85.2	81.1	444.5	284.1	466.9	288.3
APC-375	17.4	12.2	81.7	78.9	535.4	398.1	600.1	337.6
APC-560	14.2	12.0	82.8	79.2	614.9	366.4	553.6	307.3

APC-375, as expected, has the highest density of defects contributing both to weak and strong pinning (it also depicts the additional contribution of  $Gd_2O_3$  precipitates aside from BSO and grain boundaries), followed by APC-560 with less  $Gd_2O_3$ , and the reference sample having the lowest values at both 1 and 3 T. Juxtaposing both contributions, figure 10, highlights the consistent dominance of the strong pinning contribution over almost the entire temperature range. Only at 3 T, the weak pinning contribution slightly overcomes strong pinning in a narrow range at very low temperature. These results confirm that the BSO nanorods indeed act as strong pinning centers in a wide temperature range which has also led to the exemplary scaling of the pinning force shown in figure 7. At temperatures below 40 K and at higher field (i.e. 3 T compared with 1 T), the significance of the weak pinning contribution rises. This explains the less discernible peak in the  $I_c(\theta)$  due to pinning by the nanorods at lower temperatures (e.g. 30 K) and at applied fields higher than the matching field. This effect of high-field weak (or collective) pinning phase [32, 33] is generally observed in some BSO-doped REBCO films [34] and PLD-grown REBCO films with secondary phases [31, 35].

## 5. Conclusions

PLD-GdBCO coated conductors fabricated by SuperOx with and without an additional 6 mol%  $BaSnO_3$  phase were examined by STEM and transport measurements. The  $I_c(B, T, \theta)$  dependencies at intermediate temperatures between 7 and 77 K and applied magnetic field up to 6 T are used to study vortex pinning properties and their effect on the overall critical current. The APC-containing sample grown with lower deposition rate of  $375 \text{ nm min}^{-1}$  was found to contain narrow ( $5.3 \pm 2.1 \text{ nm}$ ) yet long (180–200 nm) BSO nanorods. In contrast, a faster deposition rate of  $560 \text{ nm min}^{-1}$  yielded wider ( $8.4 \pm 4.0 \text{ nm}$ ) and shorter (40–80 nm) defects. In terms of critical currents, the sample with the slower deposition rate outperforms the sample with a fast deposition rate. We analyzed the field dependence of the pinning force density ( $F_p = J_c \times B$ ) at different temperatures to obtain a better approximation of the exponent  $\alpha$  in  $I_c(B) \propto B^{-\alpha}$ . This analysis suggest that BSO nanorods indeed act as strong pinning center that enhance  $I_c$  down to temperatures below 50 K. The conclusion is further supported by the analysis of the temperature-dependence of the critical current. Below 30 K and at fields higher than 1 T, the peak in the angular dependence of  $I_c(\theta)$  related to strong pinning by the BSO nanorods

disappears, suggestive of a high-field weak (or collective) pinning phase.

## Acknowledgments

This work has received funding from the European Union's Horizon 2020 research and innovation programme ASuMED under grant agreement no. 723119. SuperOx acknowledges the support from Ministry of Science and Higher Education of Russia, Grant 075-11-2018-176.

## ORCID iDs

M Lao  <https://orcid.org/0000-0001-6101-9125>  
 R Willa  <https://orcid.org/0000-0003-1537-0824>  
 H Rijckaert  <https://orcid.org/0000-0002-6078-2919>  
 I Van Driessche  <https://orcid.org/0000-0001-5253-3325>  
 A Molodyk  <https://orcid.org/0000-0001-6313-6536>  
 J Hänisch  <https://orcid.org/0000-0003-2757-236X>

## References

- [1] Obradors X, Puig T, Palau A, Pomar A, Sandiumenge F, Mele P and Matsumoto K 2011 Nanostructured superconductors with efficient vortex pinning *Reference Module in Materials Science and Materials Engineering Comprehensive Nanoscience and Technology* ed D L Andrews et al (Amsterdam: Elsevier) ch 3.10, pp 303–49
- [2] Matsumoto K and Mele P 2010 *Supercond. Sci. Technol.* **23** 014001
- [3] Feighan J P F, Kursumovic A and MacManus-Driscoll J L 2017 *Supercond. Sci. Technol.* **30** 123001
- [4] Leroux M et al 2015 *Appl. Phys. Lett.* **107** 192601
- [5] Jia Y et al 2013 *Appl. Phys. Lett.* **103** 122601
- [6] Selvamanickam V, Gharahcheshmeh M H, Xu A, Zhang Y and Galstyan E 2015 *Supercond. Sci. Technol.* **28** 104003
- [7] Stafford B H, Sieger M, Ottolinger R, Meledin A, Strickland N M, Wimbush S C, Tendeloo G V, Hühne R and Schultz L 2017 *Supercond. Sci. Technol.* **30** 055002
- [8] Tobita H, Notoh K, Higashikawa K, Inoue M, Kiss T, Kato T, Hirayama T, Yoshizumi M, Izumi T and Shiohara Y 2012 *Supercond. Sci. Technol.* **25** 062002
- [9] Chepikov V et al 2017 *Supercond. Sci. Technol.* **30** 124001
- [10] Lee S, Petrykin V, Molodyk A, Samoilenov S, Kaul A, Vavilov A, Vysotsky V and Fetisov S 2014 *Supercond. Sci. Technol.* **27** 044022

- [11] Lao M, Hänisch J, Kauffmann-Weiss S, Gehring R, Fillinger H, Drechsler A and Holzapfel B 2019 *Rev. Sci. Instrum.* **90** 015106
- [12] Rijkaert H *et al* 2017 *Chem. Mater.* **29** 6104
- [13] Ernst Ruska-Centre for Microscopy and Spectroscopy with Electrons (ER-C) 2016 *J. Large-Scale Res. Facil.* **2** A43
- [14] Ichino Y, Yoshida Y and Miura S 2017 *Japan. J. Appl. Phys.* **56** 015601
- [15] Dew-Hughes D 1974 *Phil. Mag.* **30** 293
- [16] Long N 2013 *Entropy* **15** 2585
- [17] Long N 2013 *J. Supercond. Nov. Magn.* **26** 763
- [18] Kiss T, Matsushita T and Irie F 1999 *Supercond. Sci. Technol.* **12** 1079
- [19] Paturi P, Malmivirta M, Palonen H and Huhtinen H 2016 *IEEE Trans. Appl. Supercond.* **26** 8000705
- [20] Niel L 1992 *Cryogenics* **32** 975
- [21] Willa R, Koshelev A E, Sadovskyy I A and Glatz A 2018 *Supercond. Sci. Technol.* **31** 014001
- [22] Sadovskyy I A, Koshelev A E, Phillips C L, Karpeyev D A and Glatz A 2015 *J. Comput. Phys.* **294** 639
- [23] Koshelev A E, Sadovskyy I A, Phillips C L and Glatz A 2016 *Phys. Rev. B* **93** 060508
- [24] Willa R, Koshelev A E, Sadovskyy I A and Glatz A 2018 *Phys. Rev. B* **98** 054517
- [25] Hänisch J, Kozlova N, Cai C, Nenkov K, Fuchs G and Holzapfel B 2007 *Supercond. Sci. Technol.* **20** 228
- [26] Nakagawa H, Takamasu T, Miura N and Enomoto Y 1998 *Physica B* **246–247** 429
- [27] Nelson D and Vinokur V 1993 *Phys. Rev. B* **48** 13060
- [28] Blatter G, Feigel'man M V, Geshkenbein V B, Larkin A I and Vinokur V M 1994 *Rev. Mod. Phys.* **66** 1125
- [29] Sadovskyy I A *et al* 2016 *Adv. Mater.* **28** 4593
- [30] Palau A *et al* 2018 *Supercond. Sci. Technol.* **31** 034004
- [31] Rizzo F *et al* 2018 *Nanoscale* **10** 8187
- [32] Larkin A I and Ovchinnikov Y N 1979 *J. Low Temp. Phys.* **34** 409
- [33] Willa R, Geshkenbein V B and Blatter G 2016 *Phys. Rev. B* **93** 064515
- [34] Ko K P, Choi S M, Lee J W, Ko R K, Moon S H, Park C and Yoo S I 2014 *IEEE Trans. Appl. Supercond.* **24** 6600908
- [35] Pahlke P *et al* 2018 *Supercond. Sci. Technol.* **31** 044007